Quantifying the environmental effects on tropical cyclone intensity change using a simple dynamically based dynamical system model

Jing Xu[a,b], Yuqing Wang[c*], and Chi Yang[d]

[a]Qingdao Joint Institute of Marine Meteorology, Chinese Academy of Meteorological Sciences, China Meteorological Administration, Beijing, China

[b]State Key Laboratory of Severe Weather, Chinese Academy of Meteorological Sciences, China Meteorological Administration, Beijing, China

[c]International Pacific Research Center and Department of Atmospheric Sciences, School of Ocean and Earth Sciences, University of Hawaii at Mānoa, Honolulu, HI 96822

[d]Faculty of Geographical Science, Beijing Normal University, Beijing, China

March 31, 2023 (submitted)
August 23, 2023 (first revision)
October 12, 2023 (second revision)
Dateline

Submitted to ***Journal of the Atmospheric Sciences***

Corresponding author: Prof. Yuqing Wang
Room 404A, IPRC/SOEST
University of Hawaii at Manoa
1680 East-West Road
Honolulu, HI 96822
Email: yuqing@hawaii.edu

Abstract

Accurate prediction of tropical cyclone (TC) intensity is quite challenging due to multiple competing processes among the TC internal dynamics and the environment. Most previous studies have evaluated the environmental effects on TC intensity change from both internal dynamics and external influence. This study quantifies the environmental effects on TC intensity change using a simple dynamically based dynamical system (DBDS) model recently developed. In this simple model, the environmental effects are uniquely represented by a ventilation parameter *B*, which can be expressed as multiplicative of individual ventilation parameters of the corresponding environmental effects. Their individual ventilation parameters imply their relative importance to the bulk environmental ventilation effect and thus to the TC intensity change. Six environmental factors known to affect TC intensity change are evaluated in the DBDS model using machine learning approaches with the best-track data for TCs over the North Atlantic, central, eastern and western North Pacific and the statistical hurricane intensity prediction scheme (SHIPS) dataset during 1982–2021. Results show that the deep-layer vertical wind shear (VWS) is the dominant ventilation factor to reduce the intrinsic TC intensification rate or to drive the TC weakening, with its ventilation parameter ranging between 0.5–0.8 when environmental VWS between 200 and 850 hPa is larger than 8 m s^{-1}. Other environmental factors are generally secondary, with their respective ventilation parameters over 0.8. An interesting result is the strong dependence of the environmental effects on the stage of TC development.

1. Introduction

Understanding and accurately predicting tropical cyclones (TC) intensity change have long been challenging to both scientific research and operational forecasting (Wang and Wu 2004; Kaplan et al. 2010; Courtney et al., 2019; Hendricks et al. 2019; Tan et al. 2022). The TC intensity change is controlled by complex and nonlinear thermodynamic and dynamic processes interacting at and across multiple scales (Elsberry et al. 2013, Lin et al. 2021), which can be classified as processes intrinsic to a TC vortex and of the TC environmental (extrinsic) effects (Hendricks et.al. 2018). The effects of extrinsic and intrinsic processes on the intensity change of a TC can be complementary, amplifying, inhibiting, or offsetting (Judt and Chen, 2016). Previous studies have identified various environmental factors/processes that affect TC intensity change, such as the large-scale vertical wind shear (VWS), mid-level dry air intrusion, mid-latitude upper-level trough, the negative ocean feedback due to upwelling and vertical mixing in the upper ocean induced by the TC itself, sea surface temperature (SST) gradient, and so on (e.g., Gray 1968; DeMaria and Kaplan 1999; DeMaria et al. 2005; DeMaria 2009; Zeng et al. 2008, 2010; Tang and Emanuel 2010, 2012; Wang et al. 2015; Hendricks et.al. 2018; Fei et al. 2020; Li et al 2022).

In most previous studies, multiple linear regression has been used to identify the key environmental factors by relating the selected environmental variables and the observed TC intensity changes based on the TC best-track data (DeMaria et al. 2005). One of the problems in those statistical studies is that the intensity changes estimated include contributions not only by the environmental influences but also by the TC internal dynamics, while their respective contributions are often hard to be effectively separated and quantified. This is why the correlations between the environmental factors and the TC intensity changes are often small, and the environmental factors can only explain a small portion of the observed TC intensity changes based on the linear statistical analyses (e.g., Zeng et al. 2010; Hendricks et al. 2018). Another issue is the nonlinear interactions between the internal dynamics and external influences (Wang and Wu 2004; Elsberry et al. 2013), which could not be adequately considered by using the linear statistical methods. One such an example is the dependence of the environmental VWS effect on the stage of the TC development (e.g., Zeng et al. 2010). As a result, the potential different responses of TC intensity to environmental influences at different stages of TC development or lifetime could not be uniquely distinguished and evaluated based on the classical statistical methods.

Recently, both a simple energetically based and a dynamically based dynamical system models have been developed to quantify the intensification rate (IR) of a TC by Wang et al. (2021a, 2021b, 2022). The energetically based dynamical system (EBDS) model was formulated by viewing a TC as a Carnot heat engine, as proposed by Wang (2012, 2015) and first constructed by Ozawa and Shimokawa (2015). Wang et al. (2021a) introduced an intensity-dependent dynamical efficiency (E), instead of a constant percentage used by Ozawa and Shimokawa (2015), to quantify the conversion of the production rate of potential energy to the production rate of inner-core kinetic energy. The dynamical efficiency E depends mainly on the degree of convective organization in the eyewall and the inner-core inertial stability of the TC vortex as inferred from the balanced vortex dynamics (e.g., Schubert and Hack 1982). Therefore, in their first version of the EBDS model, Wang et al. (2021a) parameterized E as a function of the TC inner-core inertial stability. This makes the model capable of quantitatively capturing the intensity-dependence of TC IR in idealized full-physics model simulations and in observations (Wang et al. 2021a; Xu et al. 2016; Xu and Wang 2018).

The dynamically based dynamical system (DBDS) model was developed by Wang et al. (2021b) based on the slab boundary-layer entropy and tangential wind budget equations and the assumption of a thermodynamic quasi-equilibrium under the TC eyewall. A major advancement of the DBDS model of Wang et al. (2021b) compared with the earlier time-dependent theory of TC intensification developed by Emanuel (2012) is the relaxation of the moist neutral eyewall ascent by introducing an *ad hoc* parameter measuring the degree of neutrality of eyewall ascent, which depends on the TC relative intensity, namely, the current TC intensity normalized by its maximum potential intensity (MPI, Emanuel 1986). The new model was also shown to be capable of realistically capturing the intensity-dependence of TC IR in both idealized full-physics model simulations and observations (Wang et al. 2021b). Interestingly, the EBDS and DBDS models share the same mathematical formula for TC IR. The only difference is in that the dynamical efficiency E in the EBDS model is replaced by the *ad hoc* parameter (A) measuring the degree of the moist neutrality of eyewall ascent in the DBDS model. The two parameters even share the same mathematical expression, as a function of the relative TC intensity (Wang et al. 2021b).

Theoretically, without any prohibiting environmental effects, both the EBDS and DBDS models give the theoretical upper bound, or potential IR (PIR), that a TC can reach under given favorable oceanic and atmospheric environmental thermodynamic conditions and the current TC intensity (Wang et al. 2021a, b). This was recently demonstrated by Xu and Wang (2022), who showed that the EBDS model (and also the DBDS model) could skillfully reproduce the observed intensity-dependence of the 99th percentile IRs of TCs in the best-track data over the North Atlantic, central, eastern and western North Pacific during 1980–2020, indicating that the dynamical system models developed by Wang et al. (2021a, b) can reliably estimate the PIR of real TCs. More recently, the DBDS model has been extended to include the frictional dissipative heating effect by Wang et al. (2022) and refined in several aspects in Wang et al. (2023). As demonstrated by Wang et al. (2022), by including the frictional dissipative heating effect, the skill of the dynamical system model in capturing the observed TC PIR can be further improved, in particular for those extremely strong TCs in which dissipative heating can contribute positively to the PIR of intense TCs and also the TC MPI (Bister and Emanuel 1998).

Although the EBDS or DBDS model so far developed can capture the PIR of the observed TCs (Xu and Wang 2022; Wang et al. 2022) and the intensity evolution of idealized simulated TCs (Wang et al. 2021a, b), it is desirable to include the environmental effects on TC intensity change so that the theoretical model can be used to evaluate the effects of environmental factors on the observed TC intensity change, including both intensification and weakening. This is a key step toward the application of the model to TC intensity prediction. The present study attempts to extend the most recent DBDS model developed in Wang et al. (2022b) by including the environmental effects to allow the model to be used to estimate the effects of various environmental factors on TC intensity change in observations. As mentioned in Wang et al. (2021a, b), the environmental effects on TC intensity change can be included/explained by either reducing the dynamical efficiency of the TC system in the EBDS model or their ventilation effects to reduce the degree of the moist neutrality of eyewall ascent in the DBDS model, as also briefly discussed in section 2. This allows the evaluation of the environmental effects on TC intensity change, independent of the TC intensity change induced by the TC internal dynamics.

The main objectives of this study are to construct the DBDS model by including the environmental effects and to develop a generic framework based on the Gradient Boosted Decision Trees (GBDT) to quantify the relative importance of various environmental factors to the observed TC intensity change based on the TC best-track data. Instead of the use of classic linear statistical methods, this study develops a machine learning framework to objectively quantify the relative importance of various environmental factors to the observed TC intensity changes. An advantage of the framework is to allow the potential dependence of environmental influences on the stage of TC development to be considered. Machine learning, artificial neural network methods have been widely used to deal with systems that involve complex nonlinear interactions, and have been shown to improve skills of statistical TC intensity prediction schemes to some extent (e.g., Baik and Hwang 1998; Baik and Paek 2000; Lee et al. 2000; DeMaria et al. 2022; Griffin et al. 2022).

The rest of this paper is organized as follows. The modification to the DBDS model by including the environmental effects, data, and analysis methods are described in section 2. The overall environmental ventilation effect and the relative importance and contributions of various environmental factors to TC intensity change are analyzed and discussed in section 3. Case studies for Hurricanes Katrina (2005) and Jose (2017) and Typhoon Hagibis (2019) in the study period are provided in section 4 to demonstrate the validity of the results discussed in section 3. The main conclusions are given in the last section.

2. Model, data, and methodology

a. The DBDS model including the environmental effects

The DBDS model with the effect of frictional dissipative heating included recently developed by Wang et al. (2022) was extended to include the environmental ventilation effect in this study. As mentioned in section 1, Wang et al. (2022) showed that with dissipative heating included, the theoretical model can better reproduce the observed intensity-dependence of the observed PIR and also results in a high PIR for strong TCs. The simple time-dependent equation of TC intensification including the effect of dissipative heating has the following form [see Eq. (8) in Wang et al. (2022)],

$$\frac{\partial V_m}{\partial \tau} = \frac{\alpha C_D}{h}\left\{AV_{Empi}^2 - \left[1 - \gamma A\varepsilon\left(1 - \frac{\delta C_k}{2\gamma C_D}\right)\right]V_m^2\right\}, \tag{1}$$

where $\frac{\partial V_m}{\partial \tau}$ is the rate of TC intensity change with τ being time; V_m is the near-surface maximum wind speed (referred to as the TC intensity); V_{Empi} is the MPI without the dissipative heating effect included as in Emanuel (1997); α is the reduction factor of the 10-m wind speed from the depth-averaged boundary layer wind speed; C_D and C_k are the surface drag and exchange coefficients, respectively; h is the estimated depth of the well-mixed boundary layer; $\varepsilon = \frac{T_s - T_0}{T_s}$ is the thermodynamic efficiency of the Carnot heat engine (Emanuel 1986), with T_s and T_0 being the underlying SST and the outflow layer air temperature, respectively; δ is a tracking parameter to switch the possible effect of dissipative heating on surface heat flux as advocated by Edwards (2019); and γ is the percentage of the frictional dissipation converted to internal dissipative heating to warm the atmospheric surface layer; A is the an *ad hoc* parameter measuring the degree of the moist neutrality of eyewall ascent.

The MPI without considering the dissipative heating effect in Eq. (1) is given as

$$V_{Empi} = \sqrt{\frac{C_k}{C_D}\varepsilon(\kappa_o^* - \kappa_a)}, \tag{2}$$

where κ_o^* is the saturated enthalpy of the ocean surface at a given SST (T_S), κ_a the enthalpy of the atmosphere near the surface. From Eq. (1), we can get the steady-state intensity, namely the MPI with the dissipative heating effect included, as given below

$$V_{mpi} = \frac{V_{Empi}}{\sqrt{1-\gamma\varepsilon\left(1-\frac{\delta C_k}{2\gamma C_D}\right)}}. \tag{3}$$

The *ad hoc* parameter A in Eq. (1) without any unfavorable environmental effects was assumed as a function of the relative intensity in Wang et al. (2021b). They also mentioned that the unfavorable environmental effects can be introduced as a ventilation parameter that reduces the degree of moist neutrality of eyewall ascent. Namely, we can assume

$$A \cong B\left(\frac{V_m}{V_{mpi}}\right)^n, \tag{4}$$

where B is a parameter $(0 < B \leq 1)$ representing the ventilation effect of all unfavorable environmental factors, and $n = 3/2$ based on calibrations using results from idealized full-physics numerical simulations (Wang et al. 2021b) and observations using best-track data (Xu and Wang 2022). If there is no any unfavorable environmental effect, $B = 1.0$, indicating an intensifying TC can reach its PIR. Under more general conditions with various environmental effects, B (<1.0) can be decomposed into the following form,

$$B = B_1 \times B_2 \times B_3 \cdots, \tag{5}$$

where B_i $(i = 1, 2, 3, \cdots)$ is the ventilation parameter of the ith environmental factor, such as the environmental VWS, the mid-level environmental moisture, and so on (see section 2b). The main objective of this study is to determine the environmental ventilation effects using the TC best-track data and various environmental variables from the Statistical Hurricane Intensity Prediction Scheme (SHIPS) dataset and machine learning algorithm.

If not otherwise stated, all parameters through Eq. (4) and constants in the DBDS model Eq. (1) are taken the same as those used in Wang et al. (2022), except for B included in A. Namely, $\delta = 1$ and $\gamma = 0.8$ were used in this study. The effect of dissipative heating on surface heat flux is included, and 80% of work done by surface friction is converted to dissipative heating (Wang et al. 2022); and values for several other parameters are $C_D = 2.4 \times 10^{-3}$, $C_k = 1.2 \times 10^{-3}$, $h =$ 2000 m, and $\alpha = 0.75$. These were shown to give the best fits of the results from full-physics model simulations (Wang et al. 2021a, b) and observations based on TC best-track data (Xu and Wang 2022), and all are quite reasonable under TC conditions and thus will be used in our following analyses as well.

With the DBDS model introduced, in the following we present our approach to the multiplicative decomposition of B expressed by Eq. (5) and the subsequent analyses accordingly. In order to make the description easy to follow, we first present a flowchart of our approach (Fig. 1). Details can be found in the following subsections.

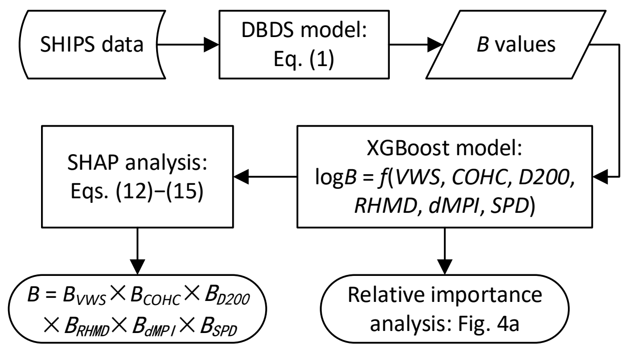

Figure 1. Workflow of the adopted approach to main objectives of this study.

b. Data

The data used in this study were obtained from the statistical hurricane intensity prediction scheme (SHIPS) database (DeMaria and Kaplan 1999; Knaff et al, 2005), which was updated on May 4, 2022. The best-track data of TCs over the North Atlantic, the central and eastern North Pacific during 1982–2021 and those over the western North Pacific during 1990–2020, were considered in our analysis. The SHIPS variables are from the Climate Forecast System Reanalysis (CFSR) for 1982-2000 but operational Global Forecast System (GFS) analyses for 2001-present for the Atlantic, eastern and central Pacific, and from CFSR from 1982-2004 and operational GFS for 2005-present for the western Pacific. The TC translation speed was calculated from the difference between the TC location changes at 6-h intervals. To minimize the influence of TC translation on its intensity, 40% of the TC translation speed was subtracted from the original 6-hourly maximum sustained 10-m wind speed for all TCs, and the result was used as the measure of TC intensity (V_m) as in Emanuel et al. (2004). The TC intensity changes at 6-h intervals were calculated accordingly ($IR_{6h} = V_m^{t+6h} - V_m^t$). Only TCs with their V_m

greater than 17 m s^{-1} were included in our analysis. Only TCs south of 35°N with tropical nature and with SST greater than 25°C were considered in our analysis to avoid extratropical transition stages. All landfalling TCs were removed. As in Xu and Wang (2022), the MPIs from the SHIPS dataset were multiplied by a factor of 1.11 with the dissipative heating effect considered as in Wang et al. (2022) to consider the superintensity nature of TCs. After such modifications, all TC MPIs were greater than or equal to their corresponding intensities in the best-track data so that no negative PIR existed for any intensifying TCs in our analysis.

Six major environmental factors in the SHIPS dataset were selected and their effects on TC intensity changes were evaluated in this study. They are the environmental VWS defined as the magnitude of the vector wind difference between 850 and 200 hPa, the climatological ocean heat content (COHC), the upper-level divergence at 200 hPa (D200), the relative humidity (RH) between 500-700 hPa averaged between 200-800 km from the TC center, and the TC translation speed. To take into account the change in SST due to TC motion (e.g., Wood and Ritchie 2015; Fei et al. 2020), the MPI difference between t_0 and $t_{0+6\mathrm{h}}$ (dMPI) is considered as a proxy. Note that the effect of environmental sounding (vertical stratification of temperature and moisture) was included in the MPI calculation using the algorithm described in Bister and Emanuel (2002) and thus was not considered as an independent environmental factor herein. Table 1 lists the TC 6-hourly maximum sustained 10-m wind speed and environmental variables/factors evaluated in this study.

TABLE 1. The factors analyzed in this study with their units and descriptions.

Variables	Units	Descriptions
V_m	m s^{-1}	Current TC intensity calculated by subtracting 40% of the translation speed from the best-track data
V_{Empi}	m s^{-1}	Maximum potential intensity (Emanuel 1986)
VWS	m s^{-1}	Deep-layer vertical wind shear defined as vector difference of winds averaged within 200-800 km between 850 and 200 hPa
COHC	kJ cm^{-2}	Climatological ocean heat content
D200	10^{7}s^{-1}	Divergence averaged within a radius of 1000 km from the TC center at 200 hPa

RHMD	%	Mean 500-700 hPa RH averaged between 200-800 km from the TC center
dMPI	m s^{-1}	MPI difference between t_0 and t_{0+6h} along TC track
SPD	m s^{-1}	Translation speed of the TC system.

c. Machine learning methods

To quantify the environmental effects as a whole and the effects of individual environmental factors, a two-stage machine learning approach was adopted: first, eXtreme Gradient Boosting (XGBoost) (Chen and Guestrin 2016) was used to build a black-box but exact model of (log) B as a multiplication of all individual ventilation components (B_i) of the six selected environmental factors; then SHapley Additive exPlanations (SHAP) technique (Lundberg et al. 2020) was used to transform the black-box model of (log) B into an additive model, equivalent to a multiplicative model of B. The final multiplicative form of B was used to quantify the effects of all individual factors.

i) XGBoost

The XGBoost algorithm is a popular implementation of boosted regression trees (Friedman, 2001). Gradient boosting optimizes a loss function by iteratively adding a set of decision trees into an ensemble. Each new tree is added sequentially such that it reduces the aggregate error from the existing ensemble of trees. At each iteration k, for the i-th sample y_i with an input feature vector $\mathbf{x}_i$, the estimate of y_i is updated by a decision tree $f^{(k)}(\mathbf{x}_i)$:

$$\hat{y}_i^{(k)} = \hat{y}_i^{(k-1)} - \alpha f^{(k)}(\mathbf{x}_i), \tag{6}$$

in which α denotes the learning rate, typically chosen to be less than 1, such that only a small portion of each new tree is added to the overall estimate at each iteration. To construct the decision tree $f^{(k)}$, the training data is split into left (I_L) and right (I_R) nodes based on its input features $\mathbf{x}$ by maximizing the loss reduction, or *gain*:

$$G = \frac{1}{2}\left[\frac{\left(\sum_{i\in I_L} g_i\right)^2}{\sum_{i\in I_L} h_i+\lambda} + \frac{\left(\sum_{i\in I_R} g_i\right)^2}{\sum_{i\in I_R} h_i+\lambda} - \frac{\left(\sum_{i\in I} g_i\right)^2}{\sum_{i\in I} h_i+\lambda}\right] - \gamma, \tag{7}$$

where λ and γ are regularization parameters controlling the model complexity, $I = I_L \cup I_R$, and g_i, h_i are the gradient and hessian, respectively, with respect to $\hat{y}_i^{(k)}$ of a differentiable loss function to be minimized (e.g., the mean-squared error).

When constructing the decision tree $f^{(k)}$, Eq. (7) is evaluated at each node to find the best possible split gain G^* among all features in the input $\mathbf{x}$. Typically a split is made if the gain exceeds a certain threshold. If no split is made, the node becomes a leaf and the optimal leaf weight w_j^* can be calculated by

$$w_j^* = -\frac{\sum_{i\in I_j} g_i}{\sum_{i\in I_j} h_i + \lambda}, \tag{8}$$

in which $j \in \{0, 1, 2, \ldots, T\}$, with T the total number of leaves in the tree. For a particular sample y_i, the optimized $f^{(k)}(\mathbf{x}_i)$ is then simply the leaf weight w_j^*, or

$$\hat{y}_i^{(k)} = \hat{y}_i^{(k-1)} - \alpha w_j^*. \tag{9}$$

A direct inference from the model fitting is the feature importance. Importance is a relative score that indicates the fractional contribution of each feature to the model performance measure, and is 100% when summed over all features. XGBoost provides a natural measure of feature importance, by first summing the gain of a feature's splits within a single tree [Eq. (7)], weighted by the number of related observations, and then averaged across all of the trees within the model. Once the model is fitted, importance is also evaluated accordingly for each feature. The XGBoost algorithm was adopted here to investigate the nonlinear relationships between the environmental ventilation parameter and environmental variables. The fitted model is much like a proxy model that encodes such relationships.

It is well-known that there is a bias/variance trade-off in machine learning. An overfitted model may have low bias but also poor predictive ability. For a more accurate prediction the model fitting must be controlled to allow some bias. However, it is less-known that high bias can also result in poor model interpretability (Lundberg et al. 2020). Low-bias models can better represent the true data-generating mechanism and depend more naturally on their input features, so that their interpretations of relationships in data are more stable and reliable. Since the purpose of this study is to make use of the XGBoost algorithm to interpret the relationship between B and various environmental factors rather than to predict B, we simply fit the model as accurate as possible for the training data, without further parameter tuning as in the usual machine learning practice.

ii) SHAP

SHAP is an additive feature attribution method that attributes values to each feature as the change in the expected model prediction when conditioning on that feature. Its main advantages are local accuracy and consistency in global model structure (Lundberg et al. 2020). Local accuracy states that when approximating the original model f (e.g., a fitted XGBoost model) for a specific input $\mathbf{x}$, the SHAP values ϕ_i for each feature i should sum up to the output $f(\mathbf{x})$:

$$f(\mathbf{x}) = \phi_0(f) + \sum_{i=1}^{M} \phi_i(f, \mathbf{x}), \tag{10}$$

i.e., the sum of feature attributions $\phi_i(f, \mathbf{x})$ matches the original model output $f(\mathbf{x})$, where $\phi_0(f) = E[f(\mathbf{X})]$ is the bias term. Consistency means that if a model changes so that some feature's contribution increases or stays the same regardless of the other inputs, that input's attribution should not decrease.

These SHAP values form an additive feature attribution measure to interpret complex machine learning models. SHAP values estimate contributions of each feature to each individual prediction. For a given predictor and a given sample, the SHAP value is the difference in the output depending on if the model is fitted with or without the predictor. For each sample, the sum of all SHAP values, plus the bias term (the overall mean of predictions), equals the prediction from the XGBoost model. The resulting matrix of SHAP values can be summarized to understand how a predictor contributes to the predictions. The mean absolute SHAP value across all samples summarizes the global feature importance, and more local model interpretation is possible through exploratory data visualizations such as scatterplots of individual predictors versus their corresponding SHAP values.

iii) Multiplicative model of B.

Combining Eqs. (1) and (3), the environmental ventilation parameter B can be calculated for all TC cases in using the TC best-track dataset, and are used as 'observations' to build a multiplicative model as Eq. (5). This is achieved by adopting the two-stage approach described above: we first fit a XGBoost model to $\log B$ instead of B, to capture the nonlinear relationship between $\log B$ and the selected environmental factors

$$\log B = f(\,VWS, COHC, D200, \cdots); \tag{11}$$

where VWS, COHC, D200, ⋯ indicate various environmental factors/parameters listed in Table 1. Then, by means of the SHAP values, Eq. (11) is assumed to have the following additive form:

$$\log B_i = G + \sum_{j=1}^{6} S_{ij}, \tag{12}$$

where G is the bias term (the overall mean of $\log B$); S_{ij} ($j = 1,2, \ldots ,6$) are SHAP values corresponding to the six features in Eq. (11) for the i^{th} sample. G is an undesirable term for reaching a multiplicative model as Eq. (5). Since all parameters in Eq. (5) are between 0 and 1, the higher the value is the weaker the ventilation effect, and vice versa. As a result, all terms in Eq. (12) should be negative. By proportionally allocating G to each SHAP value according to their global feature importance $I_j = \frac{1}{N}\sum_{i=1}^{N}\left|S_{ij}\right|$, which is the mean absolute SHAP value across all samples, we have:

$$S'_{ij} = \frac{G \times I_j}{\sum_{j=1}^{6} I_j} + S_{ij}, \tag{13}$$

so that Eq. (12) can be rewritten as:

$$\log B_i = \sum_{j=1}^{6} S'_{ij}. \tag{14}$$

Such an allocation scheme still holds the local accuracy and global consistency properties of SHAP values. Defining $S'_{ij} = \log(B_{ij})$ where $B_{ij} \in (0,1]$, and taking the exponential function of both sides of Eq. (14), we finally obtain the sample-specific multiplicative model of the environmental ventilation parameter:

$$B_i = \prod_{j=1}^{6} B_{ij}. \tag{15}$$

Note that SHAP values S_{ij} cannot be guaranteed to be all negative, and thus neither can

S'_{ij}. Consequently, for few cases with B_{ij} greater than 1 (all less than 1.2 in our analysis), we simply set such B_{ij} to be 1 in our following analysis. This does not affect the results.

3. Results

a. The characteristics of the environmental ventilation B

Figure 2 shows the calculated environmental ventilation parameter *B* in Eq. (1) against the relative intensity and compares the frequency distributions of *B* for intensifying and decaying TC cases using the 6-h TC best-track data. Since *B* is less than 1.0 for all TC cases in Fig. 2a, the environmental ventilation effect inhibits TC intensification (with IR < PIR) or makes TCs weaken (with $\partial V_m/\partial\tau < 0$). From Eqs. (1)–(4), we can get

$$\frac{\partial V_m}{\partial \tau} \geq 0, \ \text{when } B \geq \frac{\left(\frac{V_m}{V_{mpi}}\right)^{\frac{1}{2}}}{1+\gamma\varepsilon\left(1-\frac{\delta C_k}{2\gamma C_D}\right)\left[1-\left(\frac{V_m}{V_{mpi}}\right)^2\right]}, \qquad (16)$$

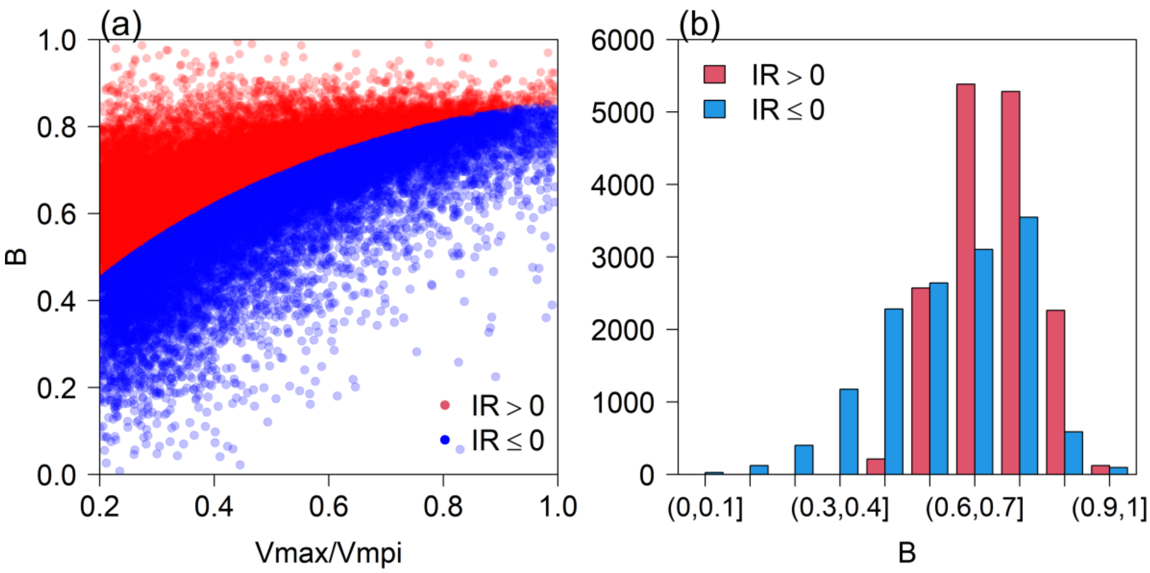

Figure 2. (a) Estimated *B* against relative intensity (V_{max}/V_{mpi}) for IR $\leqslant$ 0 (blue) and IR > 0 (red) based on the TC best-track data using Eq. (1) with $\delta = 1, \gamma = 0.8, C_k = 1.2 \times 10^{-3}$, $C_D = 2.4 \times 10^{-3}$, h = 2000 m, and α = 0.75, and (b) the frequency distributions of *B* for intensifying (red) and weakening (blue) TC cases, respectively.

Eq. (16) indicates that a TC can intensify only when the ventilation parameter related to unfavorable environmental effects exceeds a critical value. Note that stronger ventilation corresponds to smaller ventilation parameter B. The critical value depends on the relative intensity of a TC. This can be clearly seen from Fig. 2a, in which all intensifying cases (red) are located above the weakening cases (blue) for a given relative intensity. This indicates that the TC weakening results primary from strong environmental ventilation effect. From Fig. 2b, we can see that overall B is greater than 0.4, with high frequency when B is between 0.6–0.8 for intensifying cases, but B is evenly distributed for decaying cases between 0.3–0.8 with relatively high frequency when B is between 0.5–0.7, suggesting that B can well reflect the environmental ventilation effect on slowing down the TC IR or driving TC weakening. The higher B reflects the more favorable environmental conditions for TC intensification. When $B = 1$ in Eq. (4), Eq. (1) results in the PIR of an intensifying TC, indicating all environmental factors are favorable for a TC to intensify.

Figure 3 further shows the TC IR (intensifying IR > 0 and weakening IR < 0) as a function of B and relative intensity, and B as a function of IR and PIR, respectively. We can see from Fig. 3a that although IR shows a general tendency to increase with increasing B, the dependence of IR on B for intensifying TC cases is much stronger than that for weakening TC cases. Particularly, the rapid intensification (RI) cases with IR greater than 4 m $s^{-1}(6h)^{-1}$ for the 95th of all IR samples occur with B greater than 0.7. For the weakening cases, the slow weakening cases occur with B between 0.3 and 0.8, while the rapid weakening (RW) cases with IR less than -4 m $s^{-1}(6h)^{-1}$ occur with B between 0.2 and 0.7. This suggests that TCs can weaken in a large range of adverse environmental conditions. Especially, as a TC approaches its MPI at its higher relative intensity, the TC IR is very sensitive to the environmental effects. In those cases, even relatively weak environmental effects may lead to TC weakening. However, the RW cases occur with small B, indicating that RW often results from strong adverse environmental effects, such as strong environmental VWS.

The maximum IR occurs with B greater than 0.9 and relative intensity around 0.6. This is consistent with the theoretical results in Wang et al. (2021b), which showed that the theoretical maximum PIR occurs at intermediate TC intensities (roughly 60% of their MPIs). The larger negative IR [< –6 m s^{-1} (6h)$^{-1}$] occurs with B either being small (less than 0.4) when the relative intensity is relatively smaller than 0.5 or being between 0.6 and 0.7 when the relative intensity is relatively high around 0.8–0.9. This indicates that only strong adverse environmental effects can lead to RW of a TC in its primary intensification stage before reaching its maximum PIR, but relatively weak adverse environmental effects can lead to RW of a TC when it is close to its MPI as already mentioned above. This is consistent with the results by Fei et al. (2020), who statistically studied the RW of TCs over the western North Pacific and found that there were 86.1% of TCs undergoing their first weakening phase and about 29.4% of RW cases undergoing their first RW period within 24 hours after they reached their lifetime maximum intensity. The latter was recently studied in more detail by Zhou et al. (2022).

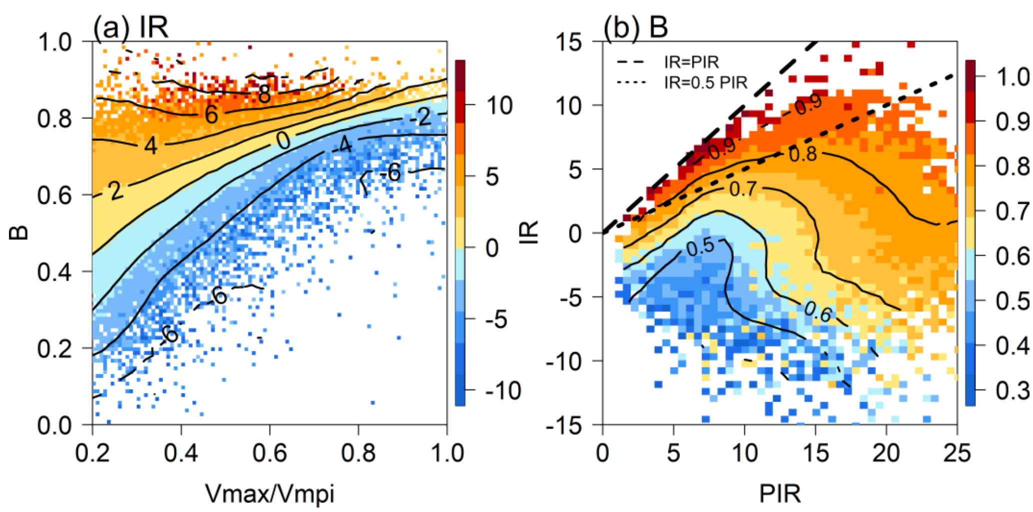

Figure 3. (a) Distribution of TC IR [m s^{-1} (6h)$^{-1}$, contours and shading] in B and relative intensity (V_{max}/V_{mpi}) space, (b) the distribution of B in IR and PIR [m s^{-1} (6h)$^{-1}$, contours and shading] space. The black dash lines in (b) denote the relative IR (namely IR normalized by the theoretical PIR) of 1.0 and 0.5, respectively.

From the distribution of B in the IR and PIR space in Fig. 3b, we can see that high B, namely favorable environmental conditions, is key for TCs reaching their PIRs. For example, intensifying TCs with their IR reaching 50% of their PIRs or above are only observed in the environment with B greater than 0.8 (short dashed line in Fig. 3b). An interesting result is the quite weak dependence of RI [with IR greater than 4 m s^{-1}(6h)$^{-1}$] on B for PIR greater than 12 m s^{-1} (6h)$^{-1}$. This indicates that TCs are potentially more resistant to the adverse environmental influence during their intensifying stage with relatively high PIRs (often with intermediate intensities as mentioned earlier, also see Wang et al. 2021a, b), but more vulnerable when their PIRs are relatively low, especially, under strong adverse environmental conditions. This indicates that the intrinsic vortex dynamics is key to TC intensification, while the adverse environmental influence controls the weakening of TCs. Furthermore, we can see that B shows a general increasing tendency with increasing IR and a decreasing tendency with the increase of IRs from their corresponding PIRs. This indicates that the adverse environmental influence plays a key role in limiting the TCs from reaching their theoretical PIR. This explains why very few TCs can reach their theoretical PIR in observations as seen in Fig. 3b.

b. XGBoost modeling and feature importance analysis of B

i) Model fitting

The environmental ventilation effect (parameter B) discussed in section 3a results from various environmental factors, such as environmental VWS, COHC, D200, RHMD, dMPI and SPD as mentioned in section 2b and listed in Table 1. In this subsection, the XGBoost model described in section 2c was used to quantify contributions of those individual environmental factors to $\log(B)$. Each environmental factor is an input feature to the XGBoost model for all TC cases. With some typical parameter settings (learning rate = 0.5 and the maximum depth of a tree = 7, refer to https://xgboost.readthedocs.io/en/latest/parameter.html for a detailed description), the root mean-square error (RMSE) of the fitted B stabilizes at 0.0023 after about 2000 iterations, which is 0.23% of the range of B. This result shows that the model with the identified input features/factors can well reproduce B through $\log(B)$. However, the fitting error does not indicate the prediction error due to the bias/variance trade-off. To examine the model's prediction skill, 10-fold cross validation of the same model was further carried out. The dataset was randomly divided into 10 subsamples with equal size, each of which was used as testing data with all the others pooled together as training data in turn for once. For each set of testing data, the mean squared error (MSE) of B predictions was calculated. In order to eliminate the potential bias caused by random division, this procedure was repeated for 10 times, yielding 100 MSEs. The root mean of these MSEs can be viewed as a measure of model prediction skill, which is 0.15 for the XGBoost model. Apparently, the prediction error is much greater than the fitting error.

Recall that, for prediction models, there is a ubiquitous trade-off between model bias and prediction variance. Linear models have the property of high bias and low variance in general (Hastie et al. 2009). We also fitted a multiple linear counterpart of the XGBoost model as a baseline for comparison:

$$E(\log(B)) = \beta_0 + \sum_{i=1}^{6} \beta_i B_i \tag{17}$$

where β_0 is the intercept and $\beta_i, i = 1, \ldots, 6$ are coefficients. Parameter estimates and their p values of significance test are shown in Table 2. It can be seen that dMPI may not be a significant linear effect at the level of 0.05 since the p value for β_5 is greater than 0.05. Using the same validation strategy, the fitting and prediction errors of B are both around 0.13. It can be seen by comparison that the fitted XGBoost model reproduces the nonlinear relationships between B and all individual environmental factors with a very small error (0.0023), much smaller than that of the counterpart linear regression model (0.13), whereas the prediction error (0.15) is a little bit larger than that of the linear model (0.13), suggesting an overfit of the XGBoost model. Since our purpose of fitting the XGBoost model is to derive a multiplicative form of B through the SHAP analysis and thus to explain which factors in B are most important, rather than to predict B for new input of environmental factors, thus an accurate or even overfitted model is acceptable.

TABLE 2. Parameter estimates and their p values for the counterpart model of Eq. (17)

Parameter	β_0 (Intercept)	β_1 (VWS)	β_2 (COHC)	β_3 (D200)	β_4 (RHMD)	β_5 (dMPI)	β_6 (SPD)
Estimate	-0.30	-8.5×10^{-4}	7.7×10^{-4}	8.5×10^{-4}	-2.4×10^{-3}	6.7×10^{-4}	3.2×10^{-3}
P values	$< 2\times10^{-16}$	$< 2\times10^{-16}$	$< 2\times10^{-16}$	$< 2\times10^{-16}$	$< 2\times10^{-16}$	0.059	$< 2\times10^{-16}$

ii) Feature importance analysis

As a direct inference of our fitted XGBoost model, the relative importance of six individual environmental factors to $\log(B)$, namely to what extent $\log(B)$ is contributed by each of the input features, are evaluated as shown in Fig. 4a. It can be seen that the environmental VWS is the most important factor and contributes 25% to $\log(B)$. Climatological ocean heat content (COHC) and the upper-level divergence (D200) contribute about 17-18% to $\log(B)$. Mid-level RH (RHMD), 6-h change in MPI along the TC track (dMPI), and translation speed (SPD) contribute, respectively, 16%, 14%, and 11% to $\log(B)$. This is broadly consistent with previous knowledge on the adverse environmental effects on TC intensity (Gray 1968; Wang and Wu 2004; Hendricks et al. 2018; Fei et al. 2020).

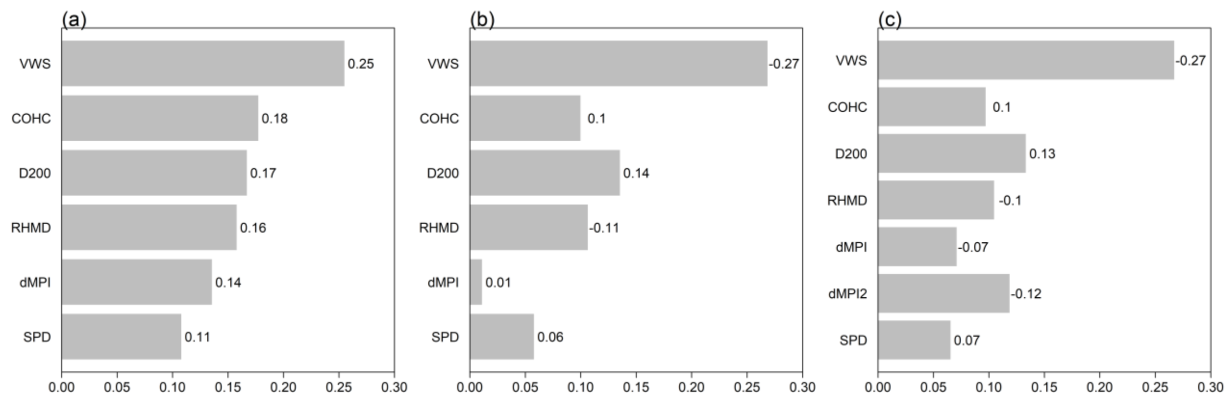

Figure 4. (a) Relative importance of six individual environmental factors used in the XGBoost model. Factors are listed to the left (see Table 1) in descending order of their relative importance. Contributions of the individual environmental factors are given on the right of their corresponding bars. (b) Same as (a) but for the counterpart linear model of (a). Bars show absolute values of SRCs with their real values labeled to the right of their corresponding bars. (c) Same as (b) but with a quadratic term dMPI2 added to the linear model.

For the counterpart linear model, however, there is not straightforward to infer the relative importance. An alternative way to check the feature importance is to examine the standardized regression coefficient (SRC) (Kleijnen and Helton, 1999)

$$SRC_i = \beta_i \frac{\sigma_i}{\sigma_Y} \tag{18}$$

where σ_i and σ_Y denote the standard deviations of the model input X_i and the model output Y, respectively. This is actually a sensitivity measure representing the expected change in Y because of an increase in X_i of one of its standardized units (i.e., σ_i), with all other X variables unchanged. The absolute values of the SRCs may be compared, giving a rough indication of the relative importance of the variables (but not weighted to sum to 1). Figure 4b shows the absolute values of SRCs of the counterpart linear model as bars with their real values labeled. Compared with Fig. 4a, VWS still has the highest relative importance; COHC, D200 and RHMD also have comparable importance values to those in Fig. 4a; dMPI, however, has the least relative importance. This result is consistent with the significance test of parameter estimates (Table 2), by which dMPI may not be a significant linear effect. This comparison suggests that dMPI exerts influence on $\log(B)$ in a nonlinear way, which has been captured by the XGBoost model. This can be confirmed simply by adding a quadratic term of dMPI (denoted as dMPI2) to the right-hand side of Eq. (17) and refitting the model. Significance tests of the parameters show that all the seven variables, including dMPI2, have significant effects with p values less than 2×10^{-16}. Relative importance of variables in the expanded model is shown in Fig. 4c. It can be seen that dMPI2 gains more importance than dMPI. However, the fitting and prediction errors of B, calculated using the same method as before, are still around 0.13: reduction in each error takes place only after the third decimal point digit is included, which is negligible. To sum up, the multiple linear regression model can only achieve very limited improvement in the model accuracy simply by adding more nonlinear terms of factors, whereas the XGBoost model can reproduce the nonlinear relationship between input factors and response almost precisely, without considerable loss of generalization ability. The latter merit is just what we require to derive the multiplicative form of B.

c. Multiplicative form of B and contributions of individual environmental factors to IR

The environmental ventilation B can be expressed as the multiplication of individual ventilation parameters B_i $(i = 1,2,\cdots,6)$ induced by the six environmental factors using the SHAP analysis described in section 2c. Figure 5 shows the six individual environmental ventilation parameters B_{VWS}, B_{COHC}, B_{D200}, B_{RHMD} B_{dMPI}, and B_{SPD} induced by, respectively, the individual environmental factors VWS, COHC, D200, RHMD, dMPI, and SPD as a function of the corresponding environmental variables and relative intensity. Overall, the relationship between each ventilation parameter and the corresponding variable is nonlinear and depends on relative intensity of TCs.

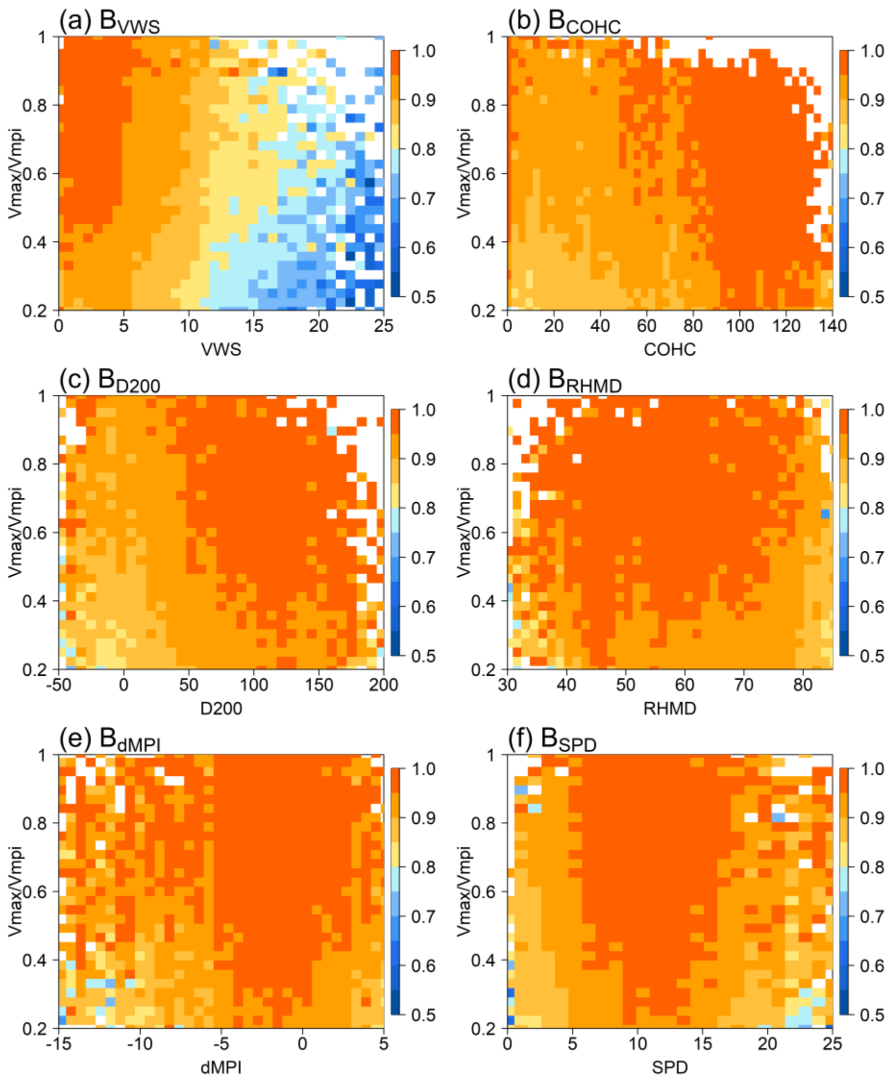

Figure 5. Individual ventilation parameters (a) B_{VWS}, (b) B_{COHC}, (c) B_{D200}, (d) B_{RHMD}, (e) B_{dMPI}, and (f) SPD induced by, respectively, VWS (m s^{-1}), COHC (kJ cm^{-2}), D200 (10^{-7} s^{-1}), RHMD (%), dMPI (m s^{-1}), and SPD (m s^{-1}) as a function of the corresponding environmental variables and relative intensity obtained using the SHAP analysis.

The ventilation parameter B_{VWS} induced by the most unfavorable environmental factor VWS varies between 0.5–1.0 (Fig. 5a). B_{VWS} is generally greater than 0.9 when VWS is less than 7m s^{-1} but decreases significantly with increasing VWS afterwards. This suggests that weak environmental VWS has very limited effect on TC intensity change but imposes an increasing adverse effect on TC IR as VWS increases beyond 8 m s^{-1}. This agrees with previously reported threshold of about 8–10 m s^{-1} above which VWS can have a significant detrimental effect on TC intensity and intensification (Zeng et al. 2010; Wang et al. 2015; Hendricks et al., 2018). B_{VWS} also shows an overall slow decrease with decreasing relative intensity, implying that environmental VWS is more detrimental to relatively weak TCs than to strong TCs. The ventilation parameters induced by other environmental factors are generally between 0.8–1.0 (Figs. 5b-5f), considerably smaller than that induced by VWS, implying that they have relatively weaker adverse effects on TC intensity change than VWS.

The ventilation parameter (B_{COHC}) induced by COHC shows a general increasing tendency with increasing COHC (Fig. 5b). This is because high ocean heat content limits the upper ocean cooling induced by upwelling and vertical mixing across the mixed layer base under the TC (Wang and Wu 2004). Similar to COHC, the ventilation parameter B_{D200} induced by upper-level divergence (D200) also varies between 0.8–1.0 (Fig. 5c). It increases with increasing upper-level divergence, suggesting that upper-level divergence (convergence) is favorable (unfavorable) for TC intensification. This is because the upper-level convergence or weak divergence is unfavorable for eyewall ascent, and thus plays a role equivalent to the mid-level ventilation induced by lateral dry-air intrusion to reduce B_{D200}. This is consistent with previous studies by Kaplan et al. (2010) and Lee et al. (2015), who found that strong upper-level environmental divergence is favorable for TC intensification.

The ventilation parameter B_{RHMD} associated with the mid-level RH between 500–700 hPa is generally high (Fig. 5d), with relatively small values for both too high (greater than 75%) and too small (less than 40%) RHMD. Too high RHMD implies moist mid-level environment, which is favorable for active rainbands and TC size expansion, which is often unfavorable for TC intensification, as demonstrated in previous modeling (e.g., Wang 2009; Hill and Lackmann 2009; Li et al. 2020) and theoretical (Wang et al. 2023) studies. In contract, too low RHMD makes the eyewall ascent vulnerable to any environmental perturbations by lateral dry-air intrusion. Therefore, too dry mid-level environment plays a role in enhancing the environmental ventilation effect (Tang and Emanuel 2010).

The factor dMPI is the change in MPI along the TC track, which is mainly determined by the underlying SST gradient and the translation speed of the TC, and determines the response timescale of the TC to change in the underlying SST. Positive dMPI partly reflects the potential increase in eyewall convection and, consequently, the weakened ventilation (Fig. 5e). Negative dMPI is equivalent to a decrease in SST, and thus increasing ventilation effect and reducing B_{dMPI}. B_{dMPI} decreases with decreasing dMPI when dMPI is less than –5 m s^{-1}. As a result, large negative dMPI often leads to rapid weakening of TCs, similar to the SST gradient previously revealed by Wood and Ritchie and (2015) and Fei et al. (2020). However, B_{dMPI} shows a decreasing trend with increasing dMPI and decreasing relative intensity for positive dMPI. This may be due to the delayed response of TC intensity to the increase in SST, which is more significant for weak TCs (with relative intensity less than 0.4).

The last factor is the TC translation speed (SPD), which has dual effects on TC intensity change and thus the ventilation parameter (B_{SPD}, Fig. 5f). On one hand, too slow translation (with SPD less than 6 m s^{-1}) often enlarges the negative ocean feedback due to cooling induced by TC forcing. On the other hand, too fast translation (with SPD greater than 20 m s^{-1}) can induce large asymmetric structure, which may lead to ventilation effect by eddy processes (Zeng et al. 2007, 2008). Note that fast translation has a more pronounced effect on weak TCs with relative intensity less than 0.4.

To further quantify contributions of individual environmental factors to TC IR ($dV_m/d\tau$), we calculated IR using Eq. (1) with A from Eq. (4) and B from Eq. (5). In each calculation, we used the actual ventilation parameter induced by one environmental factor while keeping all other ventilation factors being 1.0. For VWS as an example, the contribution by environmental VWS to TC RI (IR_{VWS}), which is calculated using the actual B_{VWS} while keeping B_{COHC}, B_{D200}, B_{RHMD}, B_{dMPI}, and B_{SPD} all being 1.0, is evaluated by IR_{VWS} normalized by the PIR calculated using Eq. (1) with B = 1 in Eq. (4). Figure 6 shows the contributions of all individual environmental factors to TC IR as a function of the factor and relative intensity. The normalized IR_{VWS} shows a nearly linear decrease with increasing VWS and also a decrease with increasing relative intensity when VWS is larger than about 7–8 m s^{-1} (Fig. 6a). This is mainly because that the stronger the TCs are when approaching their MPI, there will be lower probability for them to intensify. Note that there are a few cases with negative normalized IR_{VWS} when VWS is greater than 15 m s^{-1}, consistent with the small B_{VWS} in Fig. 5a, indicating the dominant effect of VWS on TC weakening.

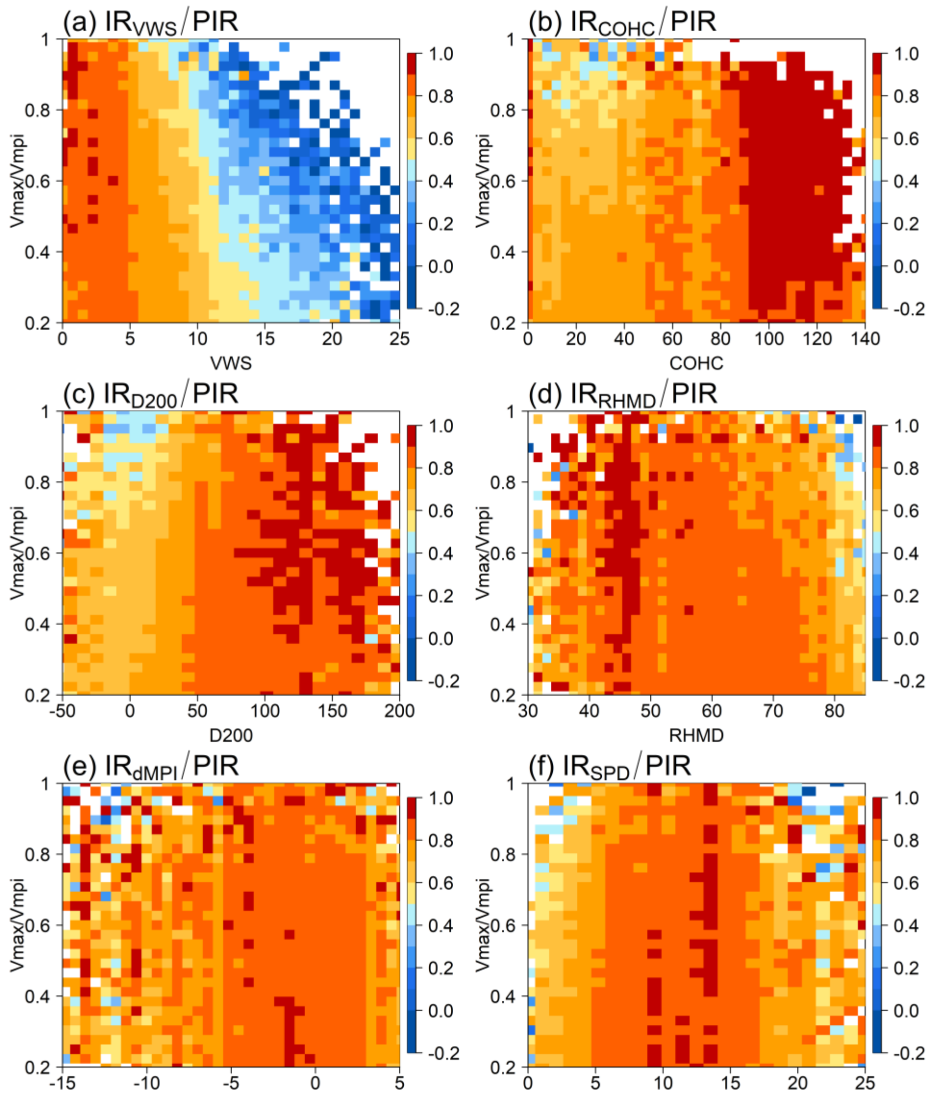

Figure 6. Same as Fig. 5, but for the normalized TC IR induced by one of individual factors to the corresponding potential intensification rate (PIR).

The normalized IR_{COHC} shows a general increase with increasing COHC (Fig. 6b), indicating that high climatological ocean heat content is favorable for TC intensification. The normalized IR_{D200} (Fig. 6c) shows somewhat small values when the D200 is convergence or weak divergence, consistent with the relatively small B_{D200} value in Fig. 5c, suggesting that upper-level environmental divergence reflects TC rapid intensification. The normalized IR_{RHMD}, IR_{dMPI}, and IR_{SPD} all show distributions in the parameter space similar to their corresponding ventilation parameters, indicating that high middle-level RH, large negative dMPI and too slow or too fast translation are all unfavorable for TC intensification. These results confirm that the environmental effects on TC IR can be effectively included in our dynamical system model through their corresponding ventilation parameters.

4. Case studies of Hurricanes Katrina (2005) and Jose (2017) and Typhoon Hagibis (2019)

In section 3, we discussed how the six environmental factors contribute to the ventilation parameter B as a whole and also individually and eventually bring the theoretical PIR towards the observed TC IR based on the DBDS model. This also makes it possible to objectively quantify the relative contributions of various environmental factors to the observed intensity change of each TC. In this section, three representative cases are used to give further insight into the environmental effects on intensity change of individual TCs in terms of their lifetime intensity changes including both intensification and weakening stages.

Before going into detailed case studies, let's first have an overview of how individual environmental factors affect B and virtually bring PIR towards IR. The six environmental ventilation parameters B_{VWS}, B_{COHC}, B_{D200}, B_{RHMD}, B_{dMPI}, and B_{SPD} for the whole sample data can be retrieved from the database discussed in section 3. Then, we calculated a set of IRs ($\partial V_m/\partial\tau$) by adding one factor each time for the six environmental effects in the above order into Eq. (1) to highlight how the PIR is reduced to the actual IR ($\partial V_m/\partial\tau$) by the six individual environmental factors, as shown in Fig. 7. Note that, theoretically, the final group of IRs (black) should coincide with real IRs such that the dots align with the diagonal line. However, due to the fitting errors from the XGBoost model propagated to the SHAP values, they scattered a bit [RMSE = 0.10 m $s^{-1}$$(6h)^{-1}$]. Also note that, different orders of adding environmental ventilation parameters do not make any difference in the black dots, which are only observable in Fig. 7.

We then retrieved the time series of the six environmental ventilation parameters B_{VWS},

B_{COHC}, B_{D200}, B_{RHMD}, B_{dMPI}, and B_{SPD} for each case individually (left column in Fig. 8), and calculated a set of IR series in the same way as done above (right column in Fig. 8). Note that the lifetime mean of individual ventilation parameters for each of the cases is given in Table 3 for a quick look at the relative contributions of individual environmental factors to the observed TC intensity changes.

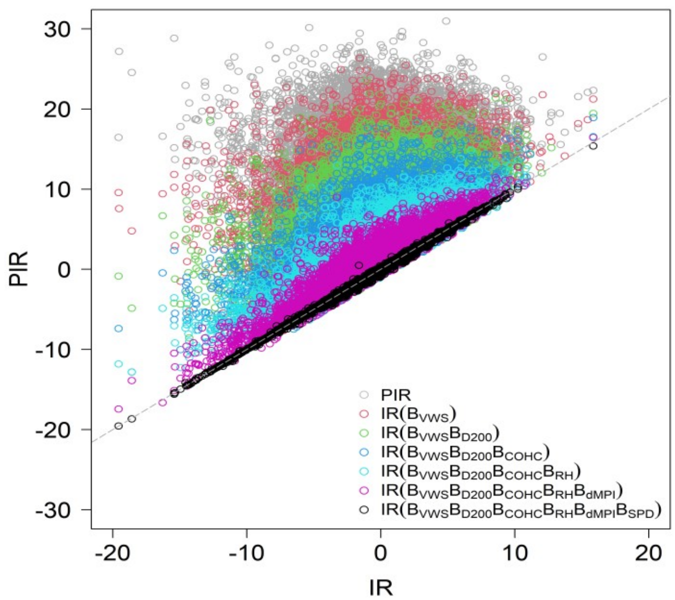

Figure 7. Illustration of how the PIR is reduced to the actual IR by adding one of the six environmental ventilation parameters for each time. The gray dashed line is diagonal.

a. Hurricane Katrina (2005)

Hurricane Katrina (2005) was one of the deadliest and the costliest meteorological disasters that struck the United States on record. Katrina formed at 1800 UTC 23 August 2005 over the southeastern Bahamas. It showed few signs of weakening during its brief passage over the Florida peninsula and began to intensify shortly after moving into the Gulf of Mexico early on 26 August. Two periods of RI on 26 and 28 August brought Katrina to category 5 with the maximum near-surface wind speed of 77 m s^{-1} (Knabb et. al. 2005). The environmental ventilation factors indicated a favorable environment for RI, such as weak VWS and large COHC with their lifetime mean ventilation parameters being 0.93 and 0.97, respectively (Table 3). Other environmental factors were also favorable for TC intensification, including moist RHMD, positive dMPI and slower SPD than average, with their ventilation parameters being 0.95–0.96 (Fig. 8a). Only D200 was a little bit weaker than normal, giving rise an average ventilation parameter of 0.91, which may hinder TC intensification (DeMaria and Kaplan 1999) until 0000 UTC 29 August. After that, the environmental VWS showed a continuous increase, leading to a rapid weakening of Katrina. Figure 8b shows how the PIR was reduced to the actual IR by adding one of the six environmental effects for each time, showing clearly that each *ad hoc* IR is indeed an upper bound on the actual IR. The weak VWS only reduced PIR slightly, while D200 was dominant in reducing PIR with the smallest B among all 6 factors (Table 3). Other factors weakened PIR slightly during the intensification stage (IR > 0), but contributed equally during the decaying stage with similar individual ventilation parameters after 1200 UTC 28 August.

b. Hurricane Jose (2017)

Hurricane Jose (2017) formed as a tropical storm by 1200 UTC 5 September west of the Cabo Verde Islands, intensified to its peak intensity of 68 m s^{-1} by 1800 UTC 8, weakened and then oscillated around 33 m s^{-1} for about five days, and then weakened to a tropical storm early on 15 September. After re-intensifying to hurricane strength in a few days, Jose weakened to a tropical storm again when it was located east of Virginia Beach and also began to take on some extratropical characteristics by 1200 UTC 19 September. Jose had a long over-water lifespan of a total of 14.75 days (Berg 2018). Along the long-life track of Jose, all environmental factors played complicated roles in its RI, intensity fluctuation, and weakening processes. Initially, both the increasing PIR and high B led to RI, making Jose attaining its lifetime maximum intensity (LMI) (Figs. 8c and 8d). Jose moved northwestward after 9 through 11 September, and suffered from an increasing northeasterly VWS and a partial eyewall replacement, which caused B_{VWS} to decrease sharply, and thus Jose weakened below hurricane intensity. For the rest of its life, environmental VWS played a dominant role during its intensity fluctuation and weakening processes. VWS was 3.4 m s^{-1} larger than normal average, resulting in a low B_{VWS} of 0.86 (Table 3), which alone reduced about 42% of the PIR (Fig. 8d).

c. Typhoon Hagibis (2019)

Super Typhoon Hagibis (2019) formed over the western North Pacific in October 2019. It intensified explosively from 28 m s^{-1} at 1200 UTC 6 to 73 m s^{-1} at 1200 UTC 7 (from tropical storm to Category 5), namely reached its LMI of 73 m s^{-1}. Hagibis started its RI and reached the maximum IR of 15.4 m s^{-1}(6h)$^{-1}$ at 1200 UTC 7, which is very close to its PIR under a favorable environment. Note that the maximum IR happened when the relative intensity (V_{max}/V_{mpi}) was around 0.54, which is consistent with observation in Fig. 3a and the theoretical results in Wang et al. (2021b), who showed that the theoretical maximum PIR occurs at intermediate TC intensities (roughly 60% of their MPIs). After the RI, Hagibis's intensity dropped and then fluctuated during 8–9 October. Actually, the environmental factors changed little during this period, with individual ventilation parameters fluctuating slightly as shown in Fig. 8e. Lin et al. (2020) compared the environmental conditions, such as the ocean eddy, environmental vertical wind shear, and mid-level relative humidity, etc., in this period with those in the RI stage. They found that some conditions, such as weak environmental VWS and warm ocean eddy were even better in this period than in the RI period. As a result, they concluded that the eyewall replacement cycle and the relatively large size expansion predominantly hindered Hagibis' further intensification. Note that Hagibis was approaching its MPI during this period with the relative intensity greater than 0.75. As we mentioned earlier, when a TC approaches its MPI, there is less potential for it to intensify, and the IR becomes very sensitive to the environmental effects (Fig. 3a). Hagibis terminated its strengthening at 0000 UTC 9, and turned northward and moved into region with much cooler SST with relatively high VWS and low-moisture environment, which led to much lower B_{VWS} and B_{OHC}, as shown in Fig. 8f. During Hagibis' weakening stage, the environmental factors reduced 116% of the PIR, changing from intensifying to weakening. Particularly, environmental VWS alone reduced about 40% of the PIR, and together with D200 and CHOC, reduced about 80% of the PIR, which dominated the whole weakening period (Fig. 8f). As Hagibis moved northward toward Japan, the COHC was –27.2 kJ cm^{-2} below the average (Table 3), which was also a major factor contributing to Hagibis' weakening process.

TABLE 3. List of environmental factors, in standard (std) anomaly form, and individual ventilation parameters *B* of lifetime mean of TCs Katrina, Jose and, Hagibis, respectively.

	Katrina	**Jose**	**Hagibis**
Factors	(std anomaly)/B	(std anomaly)/B	(std anomaly)/B
VWS	-1.11/0.93	3.4/0.86	-0.92/0.92
COHC	37.2/0.97	-3.5/0.93	-27.2/0.96
D200	-34.4/0.91	-27.2/0.94	75.4/0.97
RHMD	3.4/0.96	-6.4/0.97	1.86/0.96
dMPI	1.81/0.95	0.59/0.97	-1.1/0.97
SPD	-1.85/0.96	-0.03/0.96	3.1/0.97

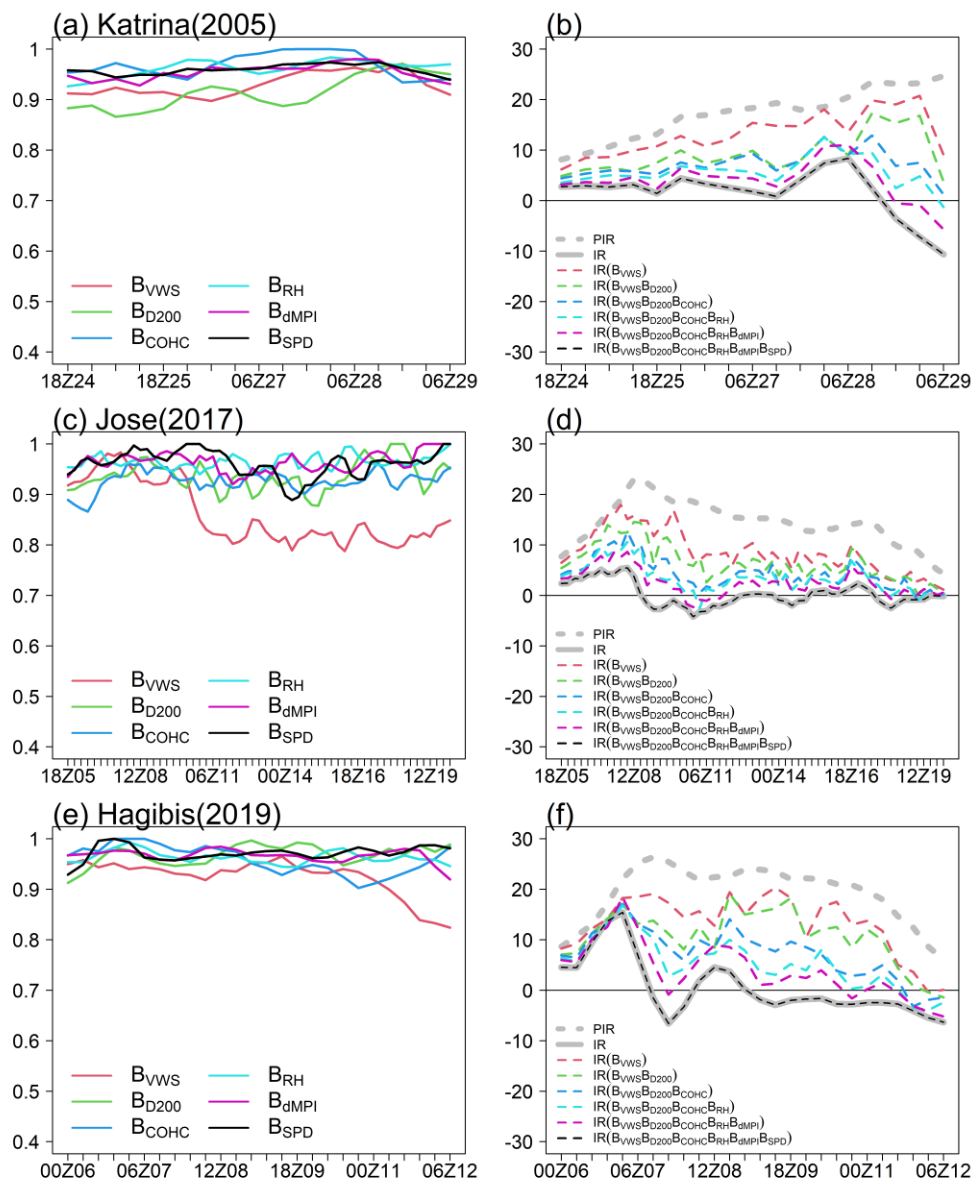

Figure 8. Case studies for Hurricanes Katrina (2005) (a and b) and Jose (2017) (c and d) and Typhoon Hagibis (2019) (e and f), respectively. The left column shows time series of the ventilation parameter B and its components due to individual environmental factors. The right column shows the PIR (grey dash, m s^{-1} day^{-1}) and reductions of the PIR by individual environmental ventilation parameters by B as the multiplication of individual ventilation parameters B_{VWS}, $B_{VWS}B_{D200}$, …, and $B_{VWS}B_{D200}B_{CHOC}B_{SPD}B_{dMPI}B_{RHMD}$ (colored dashes), respectively, towards the observed IR (grey, solid). The effect of the dominant ventilation factor VWS is highlighted by the red bold dashes for all three cases.

5. Conclusions and discussion

In two recent studies, W21a and W21b introduced a simple energetically based and a dynamically based dynamical system models, or in short EBDS and DBDS models, to quantify the intensification rate (IR) of a TC, respectively. Both models share the same mathematical expression of TC IR as a function of the relative TC intensity and maximum potential intensity (MPI). The only difference is that the dynamical efficiency (E) in the EBDS model is replaced by the *ad hoc* ventilation parameter (A) measuring the degree of the moist neutrality of eyewall ascent in the DBDS model. Both models have been shown to be capable of realistically capturing the intensity-dependence of TC IR in both idealized full-physics model simulations and observations (Wang et al. 2021b, Xu and Wang 2022). This study extends the DBDS model to include the effects of various environmental factors so that the model can be used to quantify the detrimental effects on IR of real TCs.

The environmental effect has been introduced through the environmental ventilation parameter B in the DBDS model, which can be uniquely expressed as a multiplication of individual ventilation parameters of various environmental factors. TC IR shows a general increase with increasing B or decreasing ventilation effect. Results based on the best-track data over the North Atlantic, central, eastern and western North Pacific during 1982–2021 show that the dependence of TC IR on B for intensifying TC cases is much stronger than that for weakening TC cases. Particularly, the rapid intensification [RI, with IR greater than 4 m $s^{-1}(6h)^{-1}$] cases occur with B greater than 0.7. For the weakening cases, the slow weakening cases occur with B between 0.3 and 1.0, while the rapid weakening [RW, with IR less than –4 m $s^{-1}(6h)^{-1}$] cases occur with B between 0.2 and 0.7. Especially, as a TC approaches its MPI with high relative intensity, the TC IR is very sensitive to the environmental effects. In these cases, even relatively weak environmental effects may lead to TC weakening. An interesting result is the quite weak dependence of RI on B for PIR greater than 12 m s^{-1} (6h)$^{-1}$. This indicates that TCs are potentially more resistant to the adverse environmental influence during their intensifying stage with relatively high PIRs.

Six major environmental factors in the SHIPS dataset were selected and their effects on TC intensity changes were evaluated based on the TC best-track data and the SHIPS dataset during 1982–2021, including the environmental deep-layer VWS, the climatological ocean heat content (COHC), the upper-level divergence at 200 hPa (D200), the mid-level relative humidity (RHMD) between 500–700 hPa averaged between 200–800 km from the TC center, the TC translation speed (SPD), and the MPI difference between t_0 and t_{0+6h} (dMPI) considered as a proxy of the 6-h change in SST along the TC track. The machine learning algorithm XGBoost model was adopted to quantify the relative importance of the above factors, and the SHAP method was used to quantify the contribution from each factor to the observed TC intensity change. Results from these analyses demonstrate that VWS is the most important environmental factor, which contributes 25% to $\log(B)$. COHC and D200 contribute about 17–18% to $\log(B)$. RHMD, dMPI, and SPD contribute 16%, 14%, and 11%, respectively. The ventilation parameters also represent their individual relative importance to the bulk environmental ventilation parameter and thus their relative contributions to the observed TC intensity changes.

With the SHAP analysis method, the environmental ventilation parameter B can be expressed as the multiplication of individual ventilation parameters of the selected environmental factors. Results show that the relationship between each ventilation parameter and the corresponding variable depends on the TC relative intensity. The ventilation parameter B_{VWS} induced by the environmental VWS varies between 0.5–1.0. Compared with VWS, the ventilation parameters induced by other environmental factors are relatively higher and vary between 0.8–1.0, implying that they have relatively weaker effects on TC intensity change than VWS. Consistently, the normalized IR_{VWS} decreases almost linearly with increasing VWS and also with increasing relative intensity when VWS is larger than about 7–8 m s^{-1}, largely due to the little potential for strong TCs approaching their MPI. A few cases show negative normalized IR_{VWS} when VWS is greater than 15 m s^{-1}, indicating the dominant effect of VWS on TC weakening. The normalized IR_{COHC} shows a general increase with increasing COHC indicating that high climatological ocean heat content is favorable for TC intensification. The normalized IR_{D200} shows somewhat small values when the D200 is convergence or weak divergence, suggesting that upper-level environmental divergence reflects TC rapid intensification. High RHMD, large negative dMPI, and too slow or too fast translation are all unfavorable for TC intensification.

Three representative cases, namely Hurricanes Katrina (2005) and Jose (2017) and Supertyphoon Hagibis (2019), are chosen to give further insight into the environmental effects on intensity change of individual TCs in terms of their lifetime intensity changes, including both intensification and weakening stages. Results demonstrate that the individual environmental ventilation parameters can well capture the detrimental effects of various environmental factors on TC PIR, while the relative importance of the environmental factors varied with case and the different life stages of individual TCs. In all cases, the TC weakening results primarily from strong environmental ventilation effects, with strong VWS being the major detrimental environmental factor.

We should point out that in this study it is assumed that the DBDS model can precisely give the PIR that a TC can reach under all favorable environmental thermodynamic conditions. As a result, the difference between the PIR and the observed intensity change is attributed to the detrimental environmental effects. Since the DBDS model is highly idealized and was verified based on ensemble idealized numerical simulations and best-track TC data, it could not capture the short-term intensity change resulting from high-frequency convective activities. Namely, the model can be used to evaluate the storm-scale intensification. In our study, therefore, we assumed that the best-track data mainly reflect the storm-scale intensity change. Our results strongly suggest that this assumption is acceptable. Formally the strategy we adopted here can also be used to predict the TC intensity. However, for the prediction purpose, the SHAP analysis and the multiplicative decomposition of B can be skipped, whereas more parameters tuning, validation and testing steps should be taken for developing the XGBoost model, or any other machine learning model that can model B as response to environmental factors as input features, such as neural networks. In our follow-up studies, we will apply the DBDS model to estimate the PIR and conduct real-time TC intensity prediction.

Acknowledgments: This study was supported in part by the National Key R&D Program of China under grant 2022YFC3004200, and in part by the National Natural Science Foundation of China under grants 41730960, 41875057, 41875114. YW was supported by NSF grant AGS-1834300.

Data Availability Statement

The SHIPS data are downloaded from https://rammb2.cira.colostate.edu/research/tropical-cyclones/ships/#DevelopmentalData.

References

Baik, J.J., Hwang, H.S. 1998: Tropical cyclone intensity prediction using regression method and neural network. *J. Meteorol. Soc. Jpn*., **76**, 711–717, https://doi.org/10.2151/jmsj1965.76.5_711.

Baik, J.J., Paek, J.S. 2000: A neural network model for predicting typhoon intensity. *J. Meteorol. Soc. Jpn*., **78**, 857–869, https://doi.org/10.2151/jmsj1965.78.6_857.

Berg R., 2018: National Hurricane Center tropical cyclone report: Hurricane Jose. *NOAA Rep. AL122017*, 36 pp., https://www.nhc.noaa.gov/data/tcr/AL122017_Jose.pdf.

Bister, M., and K. A. Emanuel, 1998: Dissipative heating and hurricane intensity. *Meteor. Atmos. Phys.* **50**, 233–240, https://doi.org/10.1007/BF01030791.

Bister, M., and Emanuel, K. A. 2002: Low frequency variability of tropical cyclone potential intensity, 1. Interannual to interdecadal variability. *J. Geophys. Res. – Atmos.,* **107**, 4801, https://doi.org/10.1029/2001JD000776.

Chen, T., and C. Guestrin, 2016: XGBoost: A scalable tree boosting system. Proc. 22nd ACM SIGKDD Int. Conf. on Knowledge Discovery and Data Mining, San Francisco, CA, Association for Computing Machinery, 785–794, https://doi.org/10.1145/2939672.2939785.

Courtney, J. B., Sampson, C. R., Knaff, J.A., Birchard, T., Barlow, S., Kotal, S. D., et al., 2019: Operational perspectives on tropical cyclone intensity change. Part 1: Recent advances in intensity guidance. *Trop. Cyclone Res. Rev*. **8**, 123–133. https://doi.org/10.1016/j.tcrr.2019.10.002.

Cram, T., J. Persing, M. Montgomery, and S. Braun, 2007: A Lagrangian trajectory view on transport and mixing processes between the eye, eyewall, and environment using a high-resolution simulation of Hurricane Bonnie (1998). *J. Atmos. Sci*., **64**, 1835–1856, https://doi.org/10.1175/JAS3921.1.

DeMaria, M., and Coauthors, 2022: The National Hurricane Center tropical cyclone model guidance Suite. *Wea. Forecasting*, **37**, 2141–2159, https://doi.org/10.1175/WAF-D-22-0039.1.

DeMaria, M.,1996: The effect of vertical shear on tropical cyclone intensity change, *J. Atmos. Sci*., **53**, 2076–2088, https://doi.org/10.1175/1520-0469(1996)053<2076:TEOVSO>2.0.CO;2.

DeMaria, M., and J. Kaplan, 1994: A Statistical Hurricane Intensity Prediction Scheme (SHIPS) for the Atlantic basin. *Wea. Forecasting*, **9**, 209–220, https://doi.org/10.1175/1520-0434(1994)009<0209:ASHIPS>2.0.CO;2.

DeMaria, M., and J. Kaplan, 1999: An updated statistical hurricane intensity prediction scheme (SHIPS) for the Atlantic and eastern North Pacific basins. *Wea. Forecasting*, **14**, 326–337, https://doi.org/10.1175/1520-0434(1999)014<0326:AUSHIP>2.0.CO;2.

DeMaria, M., Mainelli, M., Shay, L. K., Knaff, J. A., & Kaplan, J. 2005: Further improvements to the Statistical Hurricane Intensity Prediction Scheme (SHIPS), *Wea. Forecasting*, **20,** 531–543, https://doi.org/10.1175/WAF862.1.

Donelan, M. A., B. K. Haus, N. Reul, W. J. Plant, M. Stiassnie, H. C. Graber, O. B. Brown, and E. S. Saltzman, 2004: On the limiting aerodynamic roughness of the ocean in very strong winds. *Geophys. Res. Lett.*, **31**, L18306, https://doi.org/10.1029/ 2004GL019460.

Edwards, J. M., 2019: Sensible heat fluxes in the nearly neutral boundary layer: The impact of frictional heating within the surface layer. *J. Atmos. Sci.*, **76**, 1039–1053, https://doi.org/10.1175/JAS-D-18-0158.1.

Elsberry, L. E., L.-S. Chen, J. Davidson, R. Rogers, Y. Wang, and L. Wu, 2013: Advances in understanding and forecasting rapidly changing phenomena in tropical cyclones. Tr*opical Cyclone Res. Rev.*, **2**, 13–24, https://doi.org/10.6057/2013TCRR01.02.

Emanuel, K. A., 1986: An air–sea interaction theory for tropical cyclones. Part I: Steady-state maintenance. *J. Atmos. Sci.*, **43**, 585–604, https://doi.org/10.1175/1520–0469(1986)043<0585:AASITF>2.0.CO;2.

Emanuel, K. A., C. DesAutels, C. Holloway, and R. Korty, 2004: Environmental control of tropical cyclone intensity. *J. Atmos. Sci.*, **61**, 843–858, https://doi.org/10.1175/1520-0469(2004)061,0843:ECOTCI.2.0.CO;2.

Emanuel, K. A., 2012: Self-stratification of tropical cyclone outflow: Part II: Implications to storm intensification. *J. Atmos. Sci.*, **69**, 988–996, https://doi.org/10.1175/JAS-D-11-0177.1.

Emanuel, K. and F. Zhang, 2017: The Role of Inner-core moisture in tropical cyclone predictability and practical forecast skill. *J. Atmos. Sci.,* **74**, 2315–2324, https://doi.org/10.1175/JAS-D-17-0008.1.

Fei, R., J. Xu, Y. Wang, and C. Yang, 2020: Factors affecting the weakening rate of tropical cyclones over the Western North Pacific. *Mon. Wea. Rev.* **148**, 3693-3712, https://doi.org/10.1175/MWR-D-19-0356.1.

Friedman, J. H., 2001: Greedy function approximation: A gradient boosting machine. *Ann. Stat.*, **29**, 1189–1232, https://doi.org/10.1214/aos/1013203451.

Ge, X., and T. Li, 2013: Effects of vertical shears and midlevel dry air on tropical cyclone developments. *J. Atmos. Sci.*, **70**, 3859– 3875, https://doi.org/10.1175/JAS-D-13-066.1.

Gray, W. M., 1968: Global view of the origin of tropical disturbances and storms. *Mon. Wea. Rev.*, **96,** 669–700, https://doi.org/10.1175/1520-0493(1968)096,0669:GVOTOO.2.0.CO;2.

Griffin, S. M., A. Wimmers, and C. S. Velden, 2022: Predicting rapid intensification in North Atlantic and eastern North Pacific tropical cyclones using a convolutional neural network. *Wea. Forecasting*, **37**, 1333–1355, https://doi.org/10.1175/WAF-D-21-0194.1.

Hastie, T., R. Tibshirani, and J. Friedman, 2009: The Elements of Statistical Learning. 2nd ed. Springer, 745 pp.

Hendricks, E. A., R. L. Elsberry, C. S. Velden, A. C. Jorgensen, M. S. Jordan, and R. L. Creasey, 2018: Environmental factors and internal processes contributing to the interrupted rapid decay of Hurricane Joaquin (2015), *Wea. Forecasting*, **33**, 1251–1262, https://doi.org/10.1175/WAF-D-17-0190.1.

Hill, K. A., and G. M. Lackmann, 2009: Influence of environmental humidity on tropical cyclone size. *Mon. Wea. Rev.*, **137**, 3294–3315, https://doi.org/10.1175/2009MWR2679.1.

Judt, F., and S. S. Chen, 2016: Predictability and dynamics of tropical cyclone rapid intensification deduced from high-resolution stochastic ensembles, *Mon. Wea. Rev.*, **144,** 4395–4420, https://doi.org/10.1175/MWR-D-15-0413.1.

Kaplan, J., and J. A. Knaff, 2010: A revised tropical cyclone rapid intensification index for the Atlantic and eastern North Pacific basins. *Wea. Forecasting*, **25**, 220–241, https://doi.org/10.1175/2009WAF2222280.1.

Kleijnen, J. P. C., and J. C. Helton, 1999: Statistical analyses of scatter plots to identify important factors in large-scale simulations, 1: Review and comparison of techniques. *Reliability Engineering and System Safety*, **65(2)**, 147–185, https://doi.org/10.1016/S0951-8320(98)00091-X.

Knaff, J. A., C. R. Sampson, and M. DeMaria, 2005: An operational statistical typhoon intensity prediction scheme for the western North Pacific. *Wea. Forecasting,* **20(4)**, 688–699, https://doi.org/10.1175/WAF863.1.

Knapp, K. R., and M. C. Kruk, 2010: Quantifying interagency differences in tropical cyclone best-track wind speed estimates. *Mon. Wea. Rev.*, **138**, 1459–1473. https://doi.org/10.1175/2009MWR3123.1.

Knabb, R. D., J. R. Rhome, and D. P. Brown, 2005: Tropical cyclone report: Hurricane Katrina (23–30 August 2005). *NOAA/NHC Tech. Rep.* 43 pp. [Available online at http://www.nhc.noaa.gov/pdf/TCR-AL122005_Katrina.pdf.]

Lee, C.-Y., M. K. Tippett, S. J. Camargo, and A. H. Sobel, 2015: Probabilistic multiple linear regression modeling for tropical cyclone intensity. *Mon. Wea. Rev*., **143,** 933–954, https://doi.org/10.1175/MWR-D-14-00171.1.

Lee, R. S. T., and J. N. K. Liu, 2000: Tropical cyclone identification and tracking system using integrated neural oscillatory elastic graph matching and hybrid RBF network track mining techniques. *IEEE Trans. Neural Netw*., **11**, 680–689, https://doi.org/10.1109/72.846739.

Li, Y.-L. Y. Wang, Y.-L, Lin, and R. Fei, 2020: Dependence of superintensity of tropical cyclones on SST in axisymmetric numerical simulations. *Mon. Wea. Rev*., **148**, 4767–4781, https://doi.org/10.1175/MWR-D-20-0141.1.

Li, Y.-L., Z.-M Tan, and Y. Wang, 2022: Relative Timing of the Ends of Hurricane Intensification and Contraction of the Radius of Maximum Wind in the North Atlantic and Eastern North Pacific, *Geophys. Res. Lett.*, **49,** 1944–8007. https://doi.org/10.1029/2022GL101027.

Lin, I.-I., Rogers, R. F., Huang, H., Liao, Y., Herndon, D., Yu, J., Chang, Y., Zhang, J. A., Patricola, C. M., Pun, I., & Lien, C. 2021: A tale of two rapidly intensifying supertyphoons: Hagibis (2019) and Haiyan (2013), *Bull. Amer. Meteorol. Soc.*, **102**, E1645-E1664. https://doi.org/10.1175/BAMS-D-20-0223.1.

Lundberg, S.M., G., Erion, H. Chen, et al., 2020: From local explanations to global understanding with explainable AI for trees. *Nat. Mach. Intell.*, **2**, 56–67. https://doi.org/10.1038/s42256-019-0138-9.

Marin, J., D. Raymond, and G. Raga, 2009: Intensification of tropical cyclones in the GFS model. *Atmos. Chem. Phys.*, **9**, 1407–1417, https://doi.org/10.5194/acp-9-1407-2009.

Ozawa, H., and S. Shimokawa, 2015: Thermodynamics of a tropical cyclone: generation and dissipation of mechanical energy in a self-driven convection system. *Tellus A*, **67**, 24216, https://doi.org/10.3402/tellusa.v67.24216.

Powell, M., 1990: Boundary layer structure and dynamics in outer hurricane rainbands. Part II: Downdraft modification and mixed layer recovery. *Mon. Wea. Rev.*, **118**, 918–938, https://doi.org/10.1175/1520-0493(1990)118<0918:BLSADI>2.0.CO;2.

Riemer, M., and M. Montgomery, 2011: Simple kinematic models for the environmental interaction of tropical cyclones in vertical wind shear. *Atmos. Chem. Phys.*, **11**, 9395–9414, https://doi.org/10.5194/acp-11-9395-2011.

Riemer, M., M. Montgomery, and M. Nicholls, 2010: A new paradigm for intensity modification of tropical cyclones: Thermodynamic impact of vertical wind shear on the inflow layer. *Atmos. Chem. Phys*., **10**, 3163–3188, https://doi.org/10.5194/acp-10-3163-2010.

Rogers, R. F., and Coauthors, 2017: Rewriting the tropical record books: The extraordinary intensification of Hurricane Patricia (2015). *Bull. Amer. Meteor. Soc*., **98,** 2091–2112, https://doi.org/10.1175/BAMS-D-16-0039.1.

Rozoff, C. M., C. S. Velden, J. Kaplan, J. P. Kossin, and A. J. Wimmers, 2015: Improvements in the probabilistic prediction of tropical cyclone rapid intensification with passive microwave observations, *Wea. Forecasting*, **30,** 1016–1038. https://doi.org/10.1175/WAF-D-14-00109.1.

Simpson, R., and R. Riehl, 1958: Mid-tropospheric ventilation as a constraint on hurricane development and maintenance. Preprints, Tech. Conf. on Hurricanes, Miami Beach, FL, Amer. Meteor. Soc., D4-1–D4-10.

Tan, Z.-M., L.-L. Lei, Y. Wang, Y.-L. Xu, and Y. Zhang, 2022: Typhoon's track, intensity, and structure: from theory to prediction. *Adv. Atmos. Sci.*, **39**, 1789–1799, https://doi.org/10.1007/s00376-022-2212-1.

Tang, B., and K. Emanuel, 2010: Midlevel ventilation's constraint on tropical cyclone intensity. *J. Atmos. Sci*., **67**, 1817–1830. https://doi.org/10.1175/2010JAS3318.1.

Tang, B., and K. Emanuel, 2012: A ventilation index for tropical cyclones. *Bull. Am. Meteorol. Soc.*, **93**, 1901–1912. https://doi.org/10.1175/BAMS-D-11-00165.1.

Walker, N. D., R. R. Leben, C. T. Pilley, M. Shannon, D. C. Herndon, I.-F. Pun, I.-I. Lin, and C. L. Gentemann, 2014: Slow translational speed causes rapid collapse of northeast Pacific

Hurricane Kenneth over cold core eddy. *Geophys. Res. Lett.*, **41**, 7595–76. https://doi.org/10.1002/2014GL061584.

Wang, Y., 2009: How do outer spiral rainbands affect tropical cyclone structure and intensity? *J. Atmos. Sci*., **66**, 1250–1273, https://doi.org/10.1175/2008JAS2737.1.

Wang, Y., 2012: Recent research progress on tropical cyclone structure and intensity. *Tropical cyclone Res. Rev*., **1**, 254–275. https://doi.org/10.6057/2012TCRR02.05.

Wang, Y., 2015: Hurricane Dynamics. *Encyclopedia of Atmospheric Sciences*, 2nd edition, Vol. 6, 8–29, Gerald R. North (editor-in-chief), John Pyle and Fuqing Zhang (editors). Elsevier Ltd, https://doi.org/10.1016/B978-0-12-382225-3.00488-6.

Wang, Y., and C.-C. Wu, 2004: Current understanding of tropical cyclone structure and intensity changes-A review. *Meteor. Atmos. Phys*., **87**, 257–278, https://doi/org/10.1007/s00703-003-0055-6.

Wang, Y., Y. Rao, Z.-M. Tan, and D. Schonemann, 2015: A statistical analysis of the effects of vertical wind shear on tropical cyclone intensity change over the western North Pacific. *Mon. Wea. Rev*., **143**, 3434–3453, https://doi.org/10.1175/MWR-D-15-0049.1.

Wang, Y., Y. Li, J. Xu, Z.-M. Tan, and Y. Lin, 2021a: The intensity-dependence of tropical cyclone intensification rate in a simplified energetically based dynamical system model. *J. Atmos. Sci*., **78**, 2033–2045, https://doi.org/10.1175/JAS-D-20-0393.1.

Wang, Y., Y. Li, and J. Xu, 2021b: A new time-dependent theory of tropical cyclone intensification. *J. Atmos. Sci*., **78**, 3855–3865, https://doi.org/10.1075/JAS-D-21-0169.1.

Wang, Y., J. Xu, and Z.-M. Tan, 2022: Contribution of dissipative heating to the intensity dependence of tropical cyclone intensification, *J. Atmos. Sci.*, **79**, 2169–2180, https://doi.org/10.1175/JAS-D-22-0012.1.

Wang, Y., Z.-M. Tan, and Y. Li, 2023: Some refinements to the most recent simple time-dependent theory of tropical cyclone intensification and sensitivity. *J. Atmos. Sci.*, **79**, 321–335, https://doi.org/10.1175/JAS-D-22-0135.1.

Wood, K. M., and E. A. Ritchie, 2015: A definition for rapid weakening of North Atlantic and eastern North Pacific tropical cyclones. *Geophys. Res. Lett.*, **42**, 10,091–10,097, https://doi.org/10.1002/2015GL066697.

Xu, J., Y. Wang, and Z.-M. Tan, 2016: The relationship between sea surface temperature and maximum potential intensification rate of tropical cyclones over the North Atlantic. *J. Atmos. Sci.*, **73**, 4979–4988, https://doi.org/10.1175/JAS-D-16-0164.1.

Xu, J., and Y. Wang, 2018: Dependence of tropical cyclone intensification rate on sea surface temperature, storm intensity, and size in the western North Pacific. *Wea. Forecasting*, **33**, 523–537, https://doi.org/10.1175/WAF-D-17-0095.1.

Xu, J., and Y. Wang, 2022: Potential intensification rate of tropical cyclones in a simplified energetically based dynamical system model: An observational analysis. *J. Atmos. Sci*., **79**, 1045–1055, https://doi.org/10.1175/JAS-D-21-0217.1.

Zeng, Z.-H., L.-S. Chen, and Y. Wang, 2008: An observational study of environmental dynamical control of tropical cyclone intensity in the North Atlantic. *Mon. Wea. Rev.*, **136**, 3307–3322, https://doi.org/10.1175/2008MWR2388.1.

Zeng, Z.-H., Y. Wang, and L.-S. Chen, 2010: A statistical analysis of vertical shear effect on tropical cyclone intensity change in the North Atlantic. *Geophys. Res. Lett*., **37**, L02802, https://doi.org/10.1029/2009GL041788.

Zhang, J. A., R. F. Rogers, D. S. Nolan, and F. D. Marks, 2011: On the characteristic height scales of the hurricane boundary layer. *Mon. Wea. Rev.*, **139**, 2523–2535, https://doi.org/10.1175/MWR-D-10-05017.1.

Zhou Y.-C., R.-F. Zhan, Y. Wang, Z.-W. Wu, G.-H. Chen, and L. Wang, 2022: Characteristics and controlling factors of rapid weakening of tropical cyclones after reaching their intensity peaks over the western North Pacific. *J. Geophys. Res.: Atmos.*, **127**, e2022JD036697, https://doi.org/10.1029/2022JD036697.